Photoelectrochemical performance and ultrafast dynamics of photogenerated electrons and holes in highly titanium-doped hematite

Alexander T. Paradzah†[a], Kelebogile Maabong-Tau†[a,b], Mmantsae Diale*[a] and Tjaart P.J. Krüger *[a]

* Corresponding authors

[a] Department of Physics, University of Pretoria, Private Bag X20, Hatfield 0028, South Africa
E-mail: Mmantsae.Diale@up.ac.za, Tjaart.Kruger@up.ac.za

[b] Department of Physics, University of Botswana, Private Bag 0022, Gaborone, Botswana

† These authors contributed equally to this work.

Abstract

Elemental doping of hematite has been widely performed to improve its mobility, electrical conductivity as well as to suppress electron–hole recombination in photoelectrochemical applications. When hematite is doped with high titanium concentrations, above 5%, pseudobrookite layers may be formed as overlayers leading to improved photocurrent while further doping beyond 15% could lead to the formation of a titania overlayer which has an effect of suppressing photocurrent. In this study, we observed that doping hematite with titanium improves photocurrent, reaching a maximum of 1.83 mA cm^{-2} at a titanium concentration of 15%, the highest achieved photocurrent with spin coating method. Further titanium incorporation to 20% resulted in a decrease of the photocurrent. XRD measurements shows that a Fe_2TiO_5 layer formed at 15% Ti concentration which resulted in the observed increase in photocurrent while a reduction in photocurrent at 20% Ti concentration could have resulted from the formation of a TiO_2 layer. Analysis of the transient absorption spectroscopy data was achieved using a four-component sequential analysis scheme in the Glotaran software. We observed major doping concentration dependent lifetimes in the τ_3 and τ_4 values where the 15% doped samples had the slowest recombination rates. We also observed a blueshift in the spectra with increasing doping concentration, suggesting the occurance of the Burstein–Moss effect. This work shows that doping hematite with titanium leads to structural changes of the photoanodes at Ti concentrations of over 10%, in addition to the well documented conductivity enhancement.

1 Introduction

Increased greenhouse gas emissions and the associated global warming pose a real threat to the planet. It has thus become imperative that a transition from traditional energy sources, especially fossil fuels, be accelerated. While there are several environmentally clean sources, solar energy is the most sought after replacement for fossil fuels, due to, *inter alia*, its abundance and portability. The total global annual energy demand is exceeded by the energy that reaches the earth's surface from the sun in one hour.[1] Because of solar energy storage challenges arising from its diurnal and seasonal nature, hydrogen production from solar water

splitting is being actively pursued as it allows for better storage in the chemical bonds of the hydrogen molecules. The first demonstration of the process was illustrated by Fujishima and Honda in 1972, where they showed using a titanium dioxide (TiO_2) photoanode that sunlight can be used to decompose water into hydrogen (H_2) and oxygen (O_2) gases.[2] TiO_2 is a wide bandgap metal-oxide, thus, in its pristine form, it can only absorb substantially in the ultraviolet region of the solar spectrum. Because of this limitation, several other metal oxide semiconductors with smaller bandgaps have been explored, and these include, among others, hematite (α-Fe_2O_3), bismuth vanadate ($BiVO_4$) and tungsten trioxide (WO_3).

While small bandgap semiconductors may have an advantage of visible solar absorption over their large bandgap counterparts, they are generally associated with fast e–h recombination rates which in turn adversely limits photocurrent in photoelectrochemical cells (PECs). Small bandgap semiconductors often do not straddle the water redox potentials – a requirement for a semiconductor to perform both the reduction and oxidation processes. This, however, can be overcome by the use of a two-electrode system where the oxidation reaction takes place at the photoanode while the reduction reaction occurs at the cathode.

In this work, we focus on the use of α-Fe_2O_3 (Fe_2O_3 hereafter) as a water splitting photoanode. Fe_2O_3 has a considerably small bandgap ($\sim$2.1 eV) which enables absorption of solar photons in the visible region of the spectrum. Additionally, hematite is stable in aqueous solutions, non-toxic, and is composed of earth-abundant elements (iron and oxygen). However, Fe_2O_3 has some weaknesses such as short hole diffusion lengths, fast e–h recombination, and poor conductivity. Several methods of manipulating Fe_2O_3 have been employed to address these shortcomings. Commonly used manipulations include growing of nanoparticles rather than bulk Fe_2O_3 to address the problem of short hole diffusion lengths,[3] elemental doping to improve conductivity and mobility as well as the use of underlayers[4] and overlayers to limit e–h recombination.[5]

Elemental doping introduces extra charge carriers into the materials leading to improved conductivity. While several elements have been employed as Fe_2O_3 dopants, our focus is on the use of titanium (Ti) doping and its influence. Here Ti substitutes for Fe as Ti^{4+} and the extra of four valence electrons of Ti localizes on the nearest Fe^{3+}, thereby converting it to a localized Fe^{2+}.[6,7] The introduced Fe^{2+} is believed to improve the electron transport of Fe_2O_3 through the polaron hopping mechanism, where an electron hops from Fe^{2+} to Fe^{3+} *via* thermal activation rather than free conduction.[8,9] The improved electronic concentration and conductivity resulting from mono-dopants have been reported to be accompanied with reduced e–h recombination rates at picosecond timescales.[10] At high Ti doping levels, however, several other modifications have been reported to occur. For example, it was observed that at Ti concentrations of 5–20%, pseudobrookite (Fe_2TiO_5) and titania (TiO_2) phases begin to exist, forming overlayers.[11] The overlayers affect the photoanode either positively or negatively depending on their valence and conduction band maxima positions relative to those of Fe_2O_3.

In this study, we doped hematite with 5–20% Ti concentrations and monitored the photocurrent at each concentration. We used XRD characterization to monitor the composition of the thin films and we correlate the changes in photocurrent to the presence of new overlayers. Possible effects of the overlayers on e–h recombination rates were analyzed using ultrafast pump–probe transient absorption spectroscopy. Although the presence of overlayers has already been observed in Ti-doped hematite, here we observed the same effect and additionally explore the effect of such overlayers on e–h recombination.

2 Experimental methods

2.1 Synthesis of the electrodes

Pristine and titanium doped hematite films were prepared by spin-coating onto pre-cleaned FTO-coated glass substrates (2.2 mm substrate thickness, 600 nm FTO thickness, and FTO sheet resistance of 6.70 Ω per square) using the SM-180-BT SAWATEC spin coater, at the Laboratory for High Performance Ceramics, Swiss Federal Laboratories for Materials Science and Technology, Empa, Dübendorf in Switzerland. An iron oleate precursor complex was prepared by heating 17.0 g of oleic acid ($C_{18}H_{34}O_2$) to 125 °C using a hot plate before adding 28.0 g of iron(iii) nitrate ($Fe(NO_3)_3 \cdot 9H_2O$) in small amounts while stirring to obtain a red-brown viscous mass. The complex mixture was then cooled to room temperature and left to dry in the fume hood for 24 h. Subsequently, 70 mL of tetrahydrofuran (THF) was added to dissolve the contents followed by centrifugation at a rate of 4000 rpm for 30 minutes. The resultant supernatant solution was recovered for further processing. FTO glass substrates were cleaned by ultra-sonication in a sequence of acetone, ethanol, and deionized water (10 minutes each step), then dried with compressed nitrogen gas before use. During the deposition, small-sized precursor droplets were placed on the substrate spinning at 4000 rpm for 30 seconds, at room temperature. The thin films were annealed in a furnace at 550 °C for 30 min at 10 °C min^{-1} heating and cooling rate. Optimized three-layered thin films were obtained by repeated deposition and annealing after each layer. Ti-doping was achieved by adding titanium(iv) butoxide to the FeOOH precursor to obtain desired doping concentration levels.

2.2 Photocurrent measurements

Photocurrent measurements were carried out in a photoelectrochemical system comprising of a potentiostat (Voltalab80 PGZ 402) interfaced with a PC and a three-electrode photoelectrochemical cell. A hematite thin film was used as the working electrode while a platinum plate (0.5 × 0.5 cm) was used as the cathode, and a Ag/AgCl/(3 M KCl) electrode was employed as the reference electrode. Potassium hydroxide (KOH, 1 M) was used as the electrolyte solution. The simulated sunlight corresponded to the AM 1.5 Global solar spectrum. Photocurrent measurements were recorded from −300 to +700 mV *vs.* the Ag/AgCl electrode, at a sweep rate of 10 mV s^{-1} in darkness and under 100 mW cm^{-2} simulated light, using a solar simulator 1 Sun 300 W xenon Oriel lamp, L.O.T-Oriel AG.

2.3 Absorption and TAS measurements

Steady-state UV-Vis absorption measurements were performed using an Ocean Optics spectrometer (USB4000 series) in the ~350–800 nm wavelength region. The transient absorption spectroscopy (TAS) measurement setup has been described in detail previously.[12,13] A Ti:Sapphire amplified laser system (Clark-MXR 2110*i*) with pulse characteristics of 150 fs pulse duration, 1 kHz repetition rate and peak output centred at 775 nm was used. The output beam was split into two components: the pump beam and the probe beam. The pump beam was passed through a β-barium borate crystal for frequency doubling producing a 387.5 nm beam with a full width at half-maximum bandwidth of ~4 nm. The 387.5 nm pump beam was then directed through a neutral density filter to set the pump fluence 1.0 mJ (pulse $cm^2)^{-1}$, as measured just before the sample, then passed through a 500 Hz chopper and focussed into the sample. The probe beam was passed through a 2 ns optical delay line and focussed into a sapphire crystal for white light continuum generation. The

continuum was split into two beams, the probe beam and the reference beam. The probe was made to spatially and temporally overlap with the pump beam in the sample while a reference was also passed through the sample but without overlapping with the pump. At the sample, the pump beam was ~500 μm in diameter while the probe and reference beams were both ~300 μm. A reference beam is necessary to account for laser power fluctuations. Pump–probe measurements were carried out in the 475–660 nm wavelength range. Global analysis of the TAS data was performed using the Glotaran software to determine decay lifetimes.[14] A sequential model was used in the global analysis with four decay rates, determined from singular value decomposition analysis, giving four evolution associated difference spectra (EADS) and the associated spectral characteristics.

2.4 XRD analysis

Powder X-ray diffraction (XRD) (PAN analytical X'Pert PRO) was performed to confirm the phase, crystallinity, and structure of the thin films, and to verify the presence of pseudobrookite and titania overlayers.

3 Results and discussion

3.1 Steady-state absorption

Steady-state absorption spectra are shown in Fig. 1 for the pristine and doped samples. The samples have essentially the same absorption features and intensities through the investigated wavelength range. The absorption spectrum of hematite has been discussed previously.[13,15,16] We note from the spectra that the 20% doped sample has a slightly lower absorption intensity and this correlates well with the reduced current density as will be discussed below.
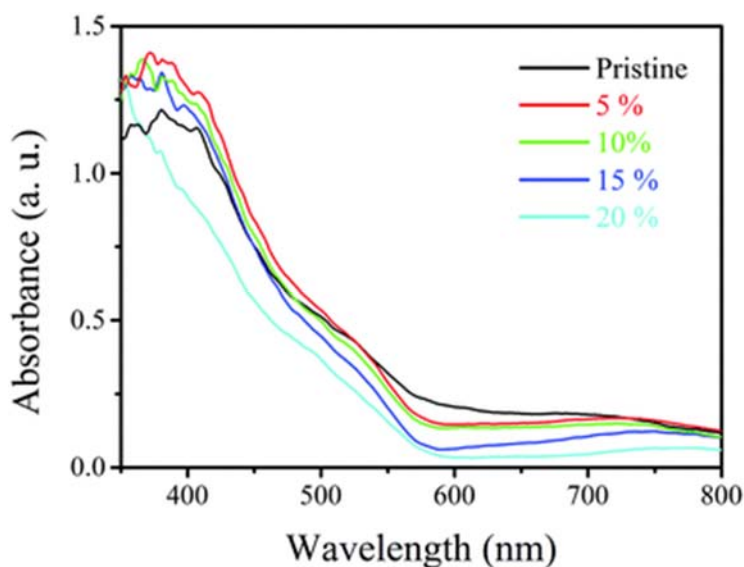

Fig. 1 Absorption spectra for the pristine and 5–20% Ti-doped hematite thin films.

3.2 Doping and photoelectrochemical performance

The PEC performance analysis of the sample was carried out by linear sweep voltammetry at 10 mV s^{-1} in 1 M KOH, in the dark and under illumination. Fig. 2 shows the measured water

oxidation photocurrent density as a function of the applied potential, for pristine and Ti-doped photoelectrodes. The pristine sample exhibited very little photocurrent with a high onset voltage of ~1.6 V. The PEC performance of the pristine film is in agreement with previous results obtained using the same preparation technique.[17] Because of relatively high binding energies in hematite, the photogenerated charge carriers in pure hematite are not spontaneously dissociated but form bound electron–hole pairs (excitons). This is a consequence of strong localized and spatially restricted electron wave functions in the conduction band, leading to increased probability of charge recombination. Nonetheless, doping of hematite with Ti^{4+} has proved to be an effective approach to reduce charge recombination rates and increase photocatalytic efficiency. Upon doping with 5–20% Ti, the overall PEC activity of the samples improved significantly, coupled with >300 mV cathodic shift of the onset potential. As the doping level increased from 0 to 15%, the photocurrent increases up to a maximum photocurrent density of ~1.82 mA cm^{-2} at 1.23 V $vs.$ RHE in the 15% sample, one the highest achieved using a chemical solution method. Interestingly, the same film showed a plateau photocurrent of ~2.44 mA cm^{-2} at 1.45 V $vs.$ RHE. In addition, the onset potential decreased significantly as compared to that of the pristine film, with that of the 5% doped sample being the lowest at ~0.95 eV $vs.$ RHE. Inset of Fig. 2 clearly shows variation of photocurrent and onset potential with titanium concentration. Although the 5% doped film required a low onset voltage compared to the 10 and 15% samples, the film produced a lower current density. The low photocurrent in the 5% doped film could be ascribed to the accumulation of holes at the surface of the photoanode due to sluggish oxygen evolution reaction kinetics. Ti-doping has been observed to enhance water splitting photocurrent at significantly lower onset potentials than pure hematite due to improved conductivity and carrier mobility, among other possibilities.[18,19] However, as the doping level increases to 20% Ti incorporation, the photocurrent decreased to levels even less than that obtained after doping at 5%, probably due to over-doping. The same Ti-doping level (0–20%) has been investigated by Monllo-Sacota et $al.$[11] for sol–gel deposited hematite. Interestingly, our 10% doping produced the same photocurrent density of 1.3 mA cm^{-2} at 1.23 V $vs.$ RHE as reported by the authors. However, in contrast, the authors observed titanium optimum doping at 10%. The difference in optimal level could be attributed to differences in preparation techniques which determine the physical properties such as morphology, crystallite size, porosity $etc.$, which in turn profoundly influence the charge transport and charge collection properties in the film. We note, however, that while our Ti-doped samples produced remarkably improved photocurrent, other semiconductor oxides have also produced even higher current densities. For instance, Zhou et $al.$[6] reported a photocurrent density of 3.2 mA cm^{-2} at 1.23 V $vs.$ RHE from $BiVO_4$ photoanodes modified using a heterometallic CoNi–MOF overlayer. Reddy et $al.$[20] also reported an even higher photocurrent density of 4.46 mA cm^{-2} at 1.23 V $vs.$ RHE from $BiVO_4$ photoanodes modified by incorporating dithiooxamide-derived N, S co-doped carbon nanosheets to act as light harvesters and also incorporating polyaniline to act as a hole transfer layer from $BiVO_4$ to CoPi. This, of course, resulted in a rather complex photoanode ($BiVO_4$-NSCN/PANI@CoPi) compared to our simplistic Ti-doped hematite photoanodes.
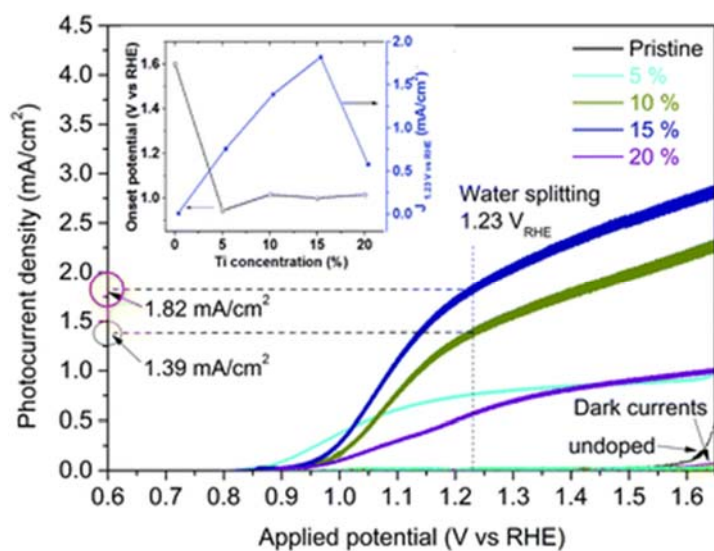
Fig. 2 Photoelectrochemical performance of hematite photoanode following different titanium concentrations. Inset figure shows variation of photocurrent and onset potential with titanium concentration.

To understand the variations in photocurrent induced upon Ti doping in the current study, we performed XRD characterization to examine the phase composition of the samples.

3.3 XRD characterization

We carried out XRD measurements both to confirm that we synthesized the right phase of iron oxide, as well as to determine if there are any new compounds, particularly after titanium incorporation, related to the observed photocurrent changes. The patterns are presented in Fig. 3. The XRD pattern of the pristine samples confirmed that we synthesized α-Fe$_2$O$_3$. Only α-Fe$_2$O$_3$ and FTO peaks were present, confirming that the sample did not contain any contaminant compounds. The same characteristic peaks were also present in the doped samples. XRD patterns of the 5 and 10% doped samples did not show significant differences from that of the pristine sample. Fig. 3 shows that the 15% and 20% doped samples contain a new diffraction peak at ~21°. This peak has been identified as a (200) plane pseudobrookite peak.[19,21,22] Similar observations were reported by Monllo-Satoca *et al.*[11] The authors confirmed through high-resolution transmission electron microscopy that, at a Ti-doping range of 15–20%, pseudobrookite and titania phases coexist but only at the surface of hematite. Considering the different changes in photocurrent at 15–20% doping in this study, it is likely that pseudobrookite (Fe$_2$TiO$_5$) was formed at 15% doping while a titania (TiO$_2$) layer formed at 20% doping, the latter which is observed by the reduced photocurrent density. The TiO$_2$ peaks are, however, not observed in our characterization. This is probably because the TiO$_2$ layer could be too thin and on the hematite surface, or coexisted as nanocrystallites as suggested by Monllor *et al.*,[11] hence are difficult to detect using XRD. In this regard, there is sufficient reason to conclude that the observed photocurrent variations induced upon doping might be related to the formation of overlayers creating hematite-pseudobrookite-TiO$_2$ heterojunctions.

6
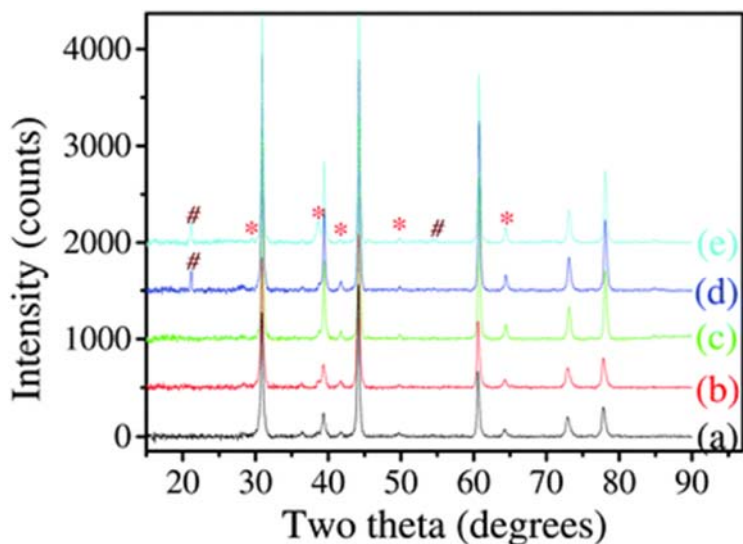
Fig. 3 X-ray diffraction patterns of: (a) pristine hematite and titanium-doped films at (b) 5%, (c) 10%, (d) 15% and (e) 20%. Hematite peaks are marked with a (*), pseudobrookite peaks with a (#) while the more prominent peaks (not labelled) belong to the FTO substrate. A Co K_{a-1} radiation source was used.

3.4 Effect of overlayers on photocurrent

The new phases, Fe_2TiO_5 and possibly TiO_2, form on the surface of hematite[11] as overlayers and thus have significant influence on the photo-electrochemical performance of the photoanodes as they form part of the semiconductor-liquid junction (SLJ) during PEC measurements. Overlayers can be beneficial to the photoanodes by extending the absorption range of the host material if their absorption range is within the visible spectrum. If, however, they absorb outside the visible region, the overlayers might not contribute positively to the solar energy absorption. Other than enhancing absorption, overlayers play an even more important role in manipulating the e–h recombination dynamics. The alignment of the energy levels in a heterostructure making the photoelectrode plays a crucial role on the charge separation and collection at the photoelectrode-electrolyte interface. A pseudo-brookite over-layer is particularly useful to hematite photoanodes because its valence band maximum is less positive than that of Fe_2O_3. This facilitates hole transfer from Fe_2O_3 to Fe_2TiO_5, thus increasing charge separation and ultimately reducing recombination in hematite. TiO_2 has an opposite effect to that of Fe_2TiO_5 in hematite photoanodes. The valence band edge of titania is more positive than that of hematite and thus a TiO_2 overlayer would keep the photogenerated holes trapped within the Fe_2O_3 and Fe_2TiO_5 layers instead of migrating to the SLJ for water oxidation. The trapping of holes within hematite by a TiO_2 overlayer leads to increased charge recombination and thus degrades the photoelectrochemical activity of the photoanode. A scheme of the bandgap positions of Fe_2O_3, Fe_2TiO_5 and TiO_2 relative to the water reduction potential is presented in Fig. 4 to graphically illustrate the influence of the respective overlayers in aiding or suppressing hole transfer to the SLJ.
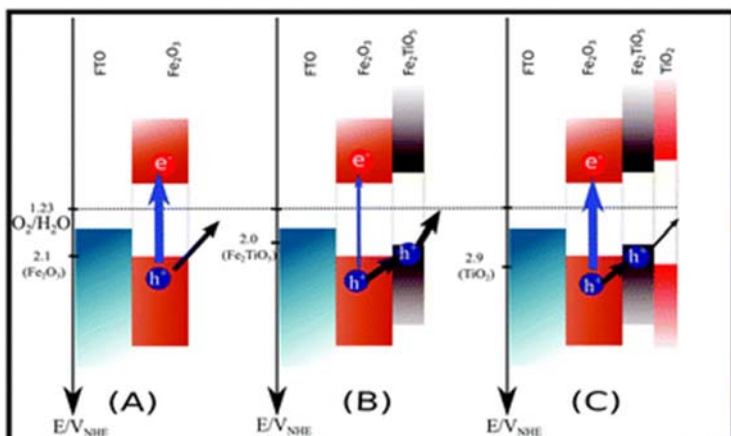
Fig. 4 Schematic representation of the conduction and valence bands of Fe_2O_3, Fe_2TiO_5 and TiO_2, and their alignments with respect to the O_2/H_2O potential. Band gap values obtained from ref. 19 and 23 and the bandgaps of Fe_2O_3, Fe_2TiO_5 and TiO_2 are 2.2, 2.2 and 3.2 eV, respectively, for determination of the conduction band minima positions. (A) Represents a case of pristine hematite where the only charge transfers are e–h recombination and hole transfer to the water semiconductor-liquid junction (SLJ). (B) Represents a possible scenario after titanium doping from 5 to 15%. Formation of a pseudobrookite overlayer is expected especially after 15% Ti doping and thus hole transfer to the SLJ is facilitated by the overlayer leading to reduced e–h recombination. (C) Represents a case where a titania overlayer is formed on top of the hematite and pseudobrookite layers, leading to reduced hole transfer and consequently increased e–h recombination. The blue arrows represent e–h recombination and the thickness is chosen to be proportional to the amount of recombination.

3.5 Ultrafast TAS

We carried out ultrafast transient absorption spectroscopy (TAS) to determine the e–h recombination rates in the photoelectrodes and also to determine the possible effects of the formed overlayers on these rates. The difference absorption spectra (ΔA) of hematite in the visible are mainly characterized by a large positive band that peaks at ~570 nm (Fig. 5). The positive band has a long tail that extends to longer wavelengths, into the IR region. The wavelength range of ~450–500 nm is characterized by a small, positive band while a negative signal is observed at wavelengths below ~450 nm. Fig. 5(a) shows a three-dimensional colour map of the pump–probe data and Fig. 5(b) shows ΔA spectra extracted at selected delay times for the pristine sample. Corresponding figures for the other samples are not shown because they follow the same trend. We have previously discussed the assignment of these spectroscopic features (positive and negative bands).[12,13] In short, the positive band that peaks at ~570 nm has been widely assigned to excited hole absorption,[24,25] while the long tail beyond 570 nm has been assigned to bandgap states assisted absorption of mainly holes but possibly also including some electron absorption.[13] Hayes *et al.*[16] however, provided experimental evidence that the peak at ~570 nm is dominated by thermal effects. They compared the optical transient absorption spectrum obtained from pump probe measurements with a thermal difference spectrum (difference of steady-state spectra obtained at 500 K and 300 K) and observed strong qualitative similarities, especially at the ~570 nm peak. Under optical transient absorption measurements, a pump pulse is expected to yield transient electron small polarons at the same time heating the lattice through carrier-phonon scattering, hence the source of optical heating in OTA measurements. Miao *et al.*[26] reconciled the different assignments by speculating that the peak could be a result of hole polarons associated with Fe^{4+} species, resulting from heat, electrical bias, or photoexcitation. The negative ΔA is believed to be a state filling induced bleach of the ground state.[24] To find the

kinetic rates of the different processes occurring after photoexcitation, we carried out global analysis of the transient absorption spectroscopy data using a four-component sequential analysis scheme. The evolution associated difference spectra obtained from the analysis are shown in Fig. S1 (ESI), and the associated decay lifetimes for each sample are displayed in Table 1.
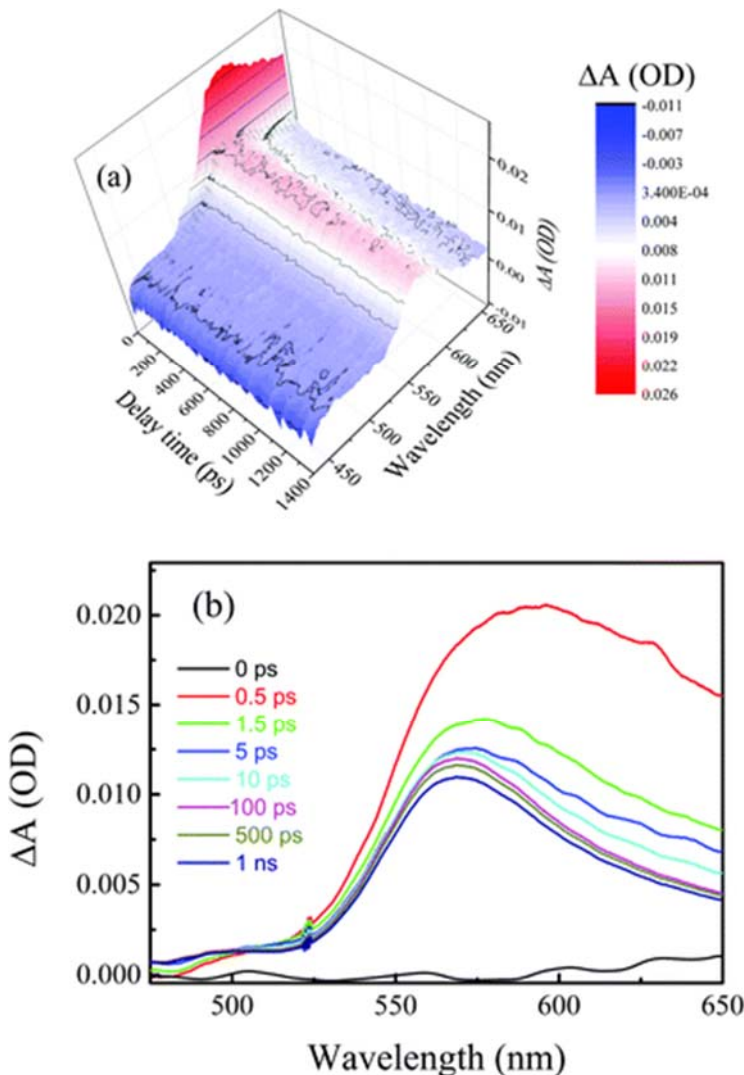
Fig. 5 (a) Three-dimensional colour map of the pristine hematite pump–probe TAS data, and (b) the difference absorption spectra at selected timescales up to 1 ns.

Table 1 Decay lifetimes obtained for the pristine and doped (5–20%) samples. Note that the maximum experimental delay time is 1300 ps, thus the accuracy of τ_4 lifetimes is dependent on the data analysis software

|	τ_1 (ps)	τ_2 (ps)	τ_3 (ps)	τ_4 (ns)
Pristine hematite	0.3	2.5	150	5.3
5% Ti	0.2	2.4	270	6.8
10% Ti	0.2	2.4	290	6.2
15% Ti	0.2	2.5	320	8.4
20% Ti	0.3	2.1	310	7.3

The values of τ_1 were sub-picosecond for all four samples and they correspond to electron and hole relaxation to the conduction and valence band edges, respectively. We used a pump

pulse centred at 3.2 eV, thus electrons were excited to energy levels above the conduction band minimum while holes can be created below the valence band maximum. These photogenerated electrons and holes then relaxed to the band edges and the processes occurred within the first picosecond post photoexcitation. The initial lifetimes were all approximately 0.3 ps or shorter. We used low fluences of 1.0 mJ (pulse cm^2)$^{-1}$, which are not expected to induce non-linear processes.[13,27,28] Such non-linear processes mainly include exciton–exciton annihilation as we have clearly demonstrated previously.[13] Three-particle Auger recombination, and biexciton formation processes may occur at very high excitation intensities but this has not been shown as yet for hematite. The second lifetimes, τ_2, did not show any dependency on Ti concentration, just like the τ_1 values. The values were in the range of 2.1–2.5 ps across the five samples. Hematite is known to contain a high density of midgap (MG) states that can trap electrons from the conduction band. The process of electron trapping by the MG states occurs at a picosecond timescale.[13] We identify the τ_2 lifetimes to represent the rate of electron trapping by the MG states. It is, however, important to note that from global analysis, the lifetimes represent rates of evolution of mixed states. It is, therefore, possible that direct band-band e–h recombination could also occur on the same timescales. The third lifetimes (τ_3) were in the range of hundreds of picoseconds and showed a clear dependence on the Ti concentration. Using target analysis, we have shown that recombination of MG trapped electrons with valence band holes occur at ~90 ps when using the same pump fluence that we used in this study.[13] The τ_3 lifetimes can, therefore, be considered to be a contribution of both direct and trap-assisted e–h recombination, leading to a longer lifetime than that resulting from pure trap-assisted recombination. The pristine sample showed the shortest τ_3 value of 150 ps while the 15% doped sample showed the longest lifetime of 320 ps. The shorter lifetime observed for the pristine sample compared to the relatively slower rates obtained for the doped samples is an indication that low conductivity is an accelerator of recombination. This is because when the conductivity is higher, there is faster separation of charges leading to suppressed recombination. The doped samples are also expected to have a higher density of Fe^{2+} electron traps compared to the pristine sample. This is because Ti^{4+} incorporation leads to the creation of an equivalent amount of Fe^{2+} cations through the reduction of Fe^{3+}. The 15% doped sample, on the other hand, showed a considerably longer lifetime than the 5 and 10% doped samples. This is possibly because the presence of a pseudobrookite layer led to increased electron transfer from hematite. This would have the effect of increasing the ratio of Fe^{2+} cation to free electron concentration, hence an increased time that an electron spends trapped, with a possibility of multiple trappings before recombination with the valence band holes. The lifetime for the 20% doped sample decreased to 310 ps, and this is conceivably because of the presence of a titania overlayer that exists at this doping level. This lifetime is, however, nearly the same as that of the 15% doped sample, suggesting that though the titania overlayer might confine charges in the pseudobrookite layer, the effect of the latter in facilitating charge separation is more dominant. Although the lifetime was shorter compared to that of the 15% doped sample, it was still longer than that of the pristine and 5-10% doped samples. This can be explained by electron transfer to the pseudobrookite layer being still possible although further transport to the SLJ is limited. The relatively faster recombination observed for the 20% Ti-doped sample is, therefore, a further indication that a titania overlayer could have formed at this doping concentration.

The fourth lifetimes (τ_4) were all on the nanosecond timescales. We attribute these lifetimes to recombination of conduction band electrons and valence band holes. It is more likely that the conduction band electrons that recombine with valence band holes at this timescale are those electrons that were previously transferred to the FTO and are transferred back to hematite through backflow. Similar to the third lifetimes, τ_4 also showed a strong dependence

10

on the doping concentrations. The pristine sample had the shortest lifetime of 5.3 ns while the 15% doped sample had the longest τ_4 value of 8.4 ns. Taking the fourth lifetimes to correspond to band-to-band electron–hole recombination, we cannot correlate these lifetimes to the presence of overlayers. It, therefore, remains to be investigated further how the longest lifetimes are related to the titanium concentration.

Fig. 6 shows clear changes in the difference absorption spectra at long delay times for different doping concentrations. Of most interest is the blue shift with increasing doping, a phenomenon known as the Burstein–Moss effect.[29] In the Burstein–Moss model, a high density of free carriers, *i.e.* photogenerated electrons and holes, will fill up the energy levels near the band edges. In the case of photogenerated electrons, subsequent optical transitions would have to involve higher energy levels, say ΔE eV above the conduction band minimum, causing an apparent increase in the bandgap, hence the observed blue shift. In this case, an increase in the doping concentration results in an increased free carrier concentration and thus a blue shift. A similar blue shift resulting from Ti doping of hematite was observed previously by Liu *et al.* following static absorption measurements.[30] The blue-shift observed by Liu *et al.* corresponds to a bandgap increase of 0.19 eV and their samples were quantum dots of 5–7 nm in size with a 5% Ti-doping concentration. In our measurements, we observe maximum blue-shift that corresponds to 0.13 eV in the 15% doped sample. While there are differences between our study and that of Liu *et al.*, the observed blue shift in both studies support the idea that hematite is easily ionized and this leads to an increase in free carrier concentration upon Ti-doping leading to an increase in the bandgap of hematite. The increase in bandgap with doping could also explain the trend observed in the third and fourth recombination lifetimes which increases with increasing Ti-concentrations, where an incrase in the bandgap leads to delayed, hence prolonged recombination rates. The red shift observed in the 20% doped sample in relation to the 15% doped sample, although not clear why it is so, does correlate with the observed trend in recombination lifetimes. The Burstein–Moss effect can also be caused by an increase in the excitonic concentration due to high pump intensities. However, in this study, the pump intensity was kept constant for both samples. Other processes that can lead to blue shifting of the ΔA spectra include an increase in the excitonic energies as a result of electrons trapped at the surface[29] and Coulombic screening by holes.[29,31]
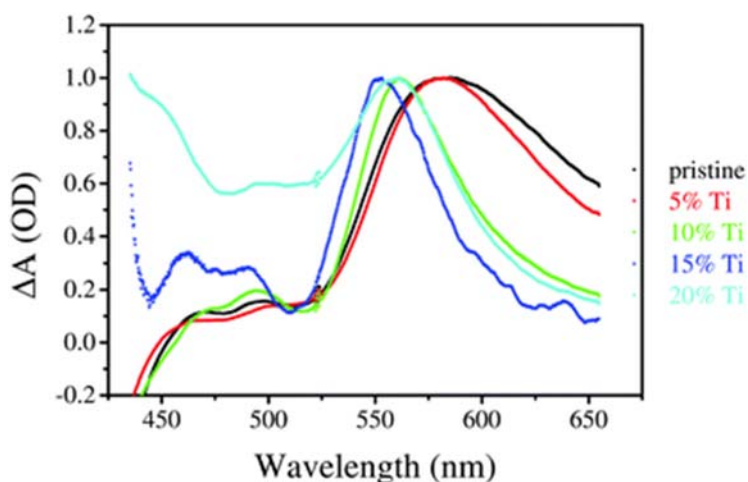
Fig. 6 Normalized 1 ns spectra for the pristine and doped (5–20%) samples.

In addition to the blue shift with increased doping concentration, some spectroscopic features appeared at higher titanium concentrations, particularly above 10% doping. These changes

are observed at shorter wavelengths where, instead of a ground-state bleach, positive signals appeared, being most pronounced for the sample doped with 20% Ti. It is not clear what the newly observed signals could be an indication of, although the most likely possibility could be that they result from the new phases, especially pseudobrookite since titania absorbs in the ultraviolet region. Although the spectroscopic signatures of pseudobrookite and titania could be different from the features we observe, a convolution of the different contributions (Fe_2O_3, TiO_2 and Fe_2TiO_5) could result in more complex spectroscopic geometries.

4 Conclusions

In summary, it was observed that incorporating titanium into hematite with concentrations of 5–15% leads to an increase in photocurrent, reaching a maximum at 15%. Further titanium concentration increase to 20% leads to a substantial decrease in the photocurrent density. XRD measurements were carried out to determine if the changes in photocurrent were resulting from thin film structural changes. It was observed that there was formation of pseudobrookite after 15% Ti doping, thus leading to the observed photocurrent enhancement. The observed suppression of photocurrent after 20% Ti doping was attributed to the formation of a titanium overlayer, even though the structural characterizations were inconclusive. The overlayers are sometimes not observable since they are likely very thin films. Ultrafast transient absorption measurements showed that the formation of pseudobrookite was associated with suppression of electron–hole recombination while the formation of a titanium layer was associated with an increase in the recombination rates. High doping concentrations were also observed to cause a blue shift in the difference absorption spectra of hematite nanostructure, indicating an increase of the bandgap – a process known as the Burstein–Moss effect. The spectroscopic signals at high titanium concentrations deviate from those of pristine hematite, further suggesting the presence of other layers, pseudobrookite and titania in particular.

Conflicts of interest

There are no conflicts to declare.

Acknowledgements

References

1. K. Rajeshwar, R. McConnell and S. Licht, *Solar hydrogen generation*, Springer, 2008
2. A. Fujishima and K. Honda, *Nature*, 1972, **238**, 37 —38 .

3. J. Brillet, M. Gratzel and K. Sivula, *Nano Lett.*, 2010, **10**, 4155 —4160
4. R. Franking, L. Li, M. A. Lukowski, F. Meng, Y. Tan, R. J. Hamers and S. Jin, *Energy Environ. Sci.*, 2013, **6**, 500 —512
5. L. Steier, I. Herraiz-Cardona, S. Gimenez, F. Fabregat-Santiago, J. Bisquert, S. D. Tilley and M. Grätzel, *Adv. Funct. Mater.*, 2014, **24**, 7681 —7688
6. A. Bandyopadhyay, J. Velev, W. Butler, S. K. Sarker and O. Bengone, *Phys. Rev. B: Condens. Matter Mater. Phys.*, 2004, **69**, 174429
7. J. Velev, A. Bandyopadhyay, W. Butler and S. Sarker, *Phys. Rev. B: Condens. Matter Mater. Phys.*, 2005, **71**, 205208
8. A. Annamalai, H. H. Lee, S. H. Choi, S. Y. Lee, E. Gracia-Espino, A. Subramanian, J. Park, K.-J. Kong and J. S. Jang, *Sci. Rep.*, 2016, **6**, 23183 —23194
9. N. Uekawa, M. Watanabe, K. Kaneko and F. Mizukami, *J. Chem. Soc., Faraday Trans.*, 1995, **91**, 2161 —2166
10. J. Deng, J. Zhong, A. Pu, D. Zhang, M. Li, X. Sun and S.-T. Lee, *J. Appl. Phys.*, 2012, **112**, 084312
11. D. Monllor-Satoca, M. Bärtsch, C. Fàbrega, A. Genç, S. Reinhard, T. Andreu, J. Arbiol, M. Niederberger and J. R. Morante, *Energy Environ. Sci.*, 2015, **8**, 3242 —3254
12. A. T. Paradzah, M. Diale, K. Maabong and T. P. Krüger, *Phys. B*, 2018, **535**, 138 —142   .
13. A. T. Paradzah, K. D. Maabong, H. M. A. M. Elnour, A. Singh, M. Diale and T. P. J. Krüger, *J. Phys. Chem. C*, 2019, **123**, 18676 —18684
14. J. Snellenburg, S. Laptenok, R. Seger, K. Mullen and I. Van Stokkum, *J. Stat. Softw.*, 2012, **49**, 1 —22
15. L. A. Marusak, R. Messier and W. B. White, *J. Phys. Chem. Solids*, 1980, **41**, 981 —984
16. D. Hayes, R. G. Hadt, J. D. Emery, A. A. Cordones, A. B. Martinson, M. L. Shelby, K. A. Fransted, P. D. Dahlberg, J. Hong and X. Zhang, *et al.*, *Energy Environ. Sci.*, 2016, **9**, 3754 —3769
17. F. L. Souza, K. P. Lopes, P. A. Nascente and E. R. Leite, *Sol. Energy Mater. Sol. Cells*, 2009, **93**, 362 —368
18. A. G. Tamirat, J. Rick, A. A. Dubale, W.-N. Su and B.-J. Hwang, *Nanoscale Horiz.*, 2016, **1**, 243 —267
19. E. Courtin, G. Baldinozzi, M. T. Sougrati, L. Stievano, C. Sanchez and C. Laberty-Robert, *J. Mater. Chem. A*, 2014, **2**, 6567 —6577.
20. D. A. Reddy, Y. Kim, H. S. Shim, K. A. J. Reddy, M. Gopannagari, D. Praveen Kumar, J. K. Song and T. K. Kim, *ACS Appl. Energy Mater.*, 2020, **3**, 4474 —4483.
21. Z. Lou, Y. Li, H. Song, Z. Ye and L. Zhu, *RSC Adv.*, 2016, **6**, 45343 —45348
22. G. Seitz, N. Penin, L. Decoux, A. Wattiaux, M. Duttine and M. Gaudon, *Inorg. Chem.*, 2016, **55**, 2499 —2507
23. R. I. Bickley, T. Gonzalez-Carreño, A. R. Gonzalez-Elipé, G. Munuera and L. Palmisano, *J. Chem. Soc., Faraday Trans.*, 1994, **90**, 2257 —2264
24. Z. Huang, Y. Lin, X. Xiang, W. Rodrguez-Córdoba, K. J. McDonald, K. S. Hagen, K.-S. Choi, B. S. Brunschwig, D. G. Musaev and C. L. Hill, *et al.*, *Energy Environ. Sci.*, 2012, **5**, 8923 —8926
25. S. R. Pendlebury, M. Barroso, A. J. Cowan, K. Sivula, J. Tang, M. Grätzel, D. Klug and J. R. Durrant, *Chem. Commun.*, 2011, **47**, 716 —718
26. T. J. Miao and J. Tang, *J. Chem. Phys.*, 2020, **152**, 194201 N. J. Cherepy, D. B. Liston, J. A. Lovejoy, H. Deng and J. Z. Zhang, *J. Phys. Chem. B*, 1998, **102**, 770 —776.

27. S. Sorenson, E. Driscoll, S. Haghighat and J. M. Dawlaty, *J. Phys. Chem. C*, 2014, **118**, 23621 —23626
28. P. V. Kamat, N. M. Dimitrijevic and A. Nozik, *J. Phys. Chem.*, 1989, **93**, 2873 — 2875
29. J. Liu, C. Liang, H. Zhang, Z. Tian and S. Zhang, *J. Phys. Chem. C*, 2012, **116**, 4986 —4992
30. L. Banyai and S. W. Koch, *Phys. Rev. Lett.*, 1986, **57**, 2722 —2724